Photon Monte Carlo Simulation for Radiative Transfer in Gaseous Media Represented by Discrete Particle Fields

Anquan Wang
Mem. ASME

Michael F. Modest[1]
Fellow ASME
e-mail: mfm6@psu.edu

Department of Mechanical and Nuclear Engineering,
Pennsylvania State University,
University Park, PA 16802

Monte Carlo ray-tracing schemes have been developed for the evaluation of radiative heat transfer for problems, in which the participating medium is represented by discrete point masses, such as the flow field and scalar fields in PDF Monte Carlo methods frequently used in combustion modeling. Photon ray tracing in such cases requires that an optical thickness is assigned to each of the point masses. Two approaches are discussed, the point particle model (PPM), in which the shape of particle is not specified, and the spherical particle model (SPM) in which particles are assumed to be spheres with specified radiation properties across their volumes. Another issue for ray tracing in particle fields is the influence region of a ray. Two ways of modeling a ray are proposed. In the first, each ray is treated as a standard volume-less line. In the other approach, the ray is assigned a small solid angle, and is thus treated as a cone with a decaying influence function away from its centerline. Based on these models, three different interaction schemes between rays and particles are proposed, i.e., line-SPM, cone-PPM and cone-SPM methods, and are compared employing several test problems.
[DOI: 10.1115/1.2345431]

1 Introduction

Among radiative transfer models, Monte Carlo ray tracing (MCRT) can be applied to problems of arbitrary difficulty with relative ease [1]. The MCRT method directly simulates the physical processes, i.e., emission, absorption, scattering, and reflection, from which the radiative transfer equation is derived.

In the standard Monte Carlo method a ray carrying a fixed amount of energy is emitted and its progress is then traced until it is absorbed at a certain point in the participating medium or at the wall, or until it escapes from the enclosure. As many researchers have pointed out [2–6], this method is inefficient when the walls are highly reflective and/or the medium is optically thin so that most photon bundles exit the enclosure without any contribution to the statistics. Modest [4,5] applied the concept of energy partitioning to alleviate this problem. In this method the energy carried by a ray is not absorbed at a single point, but rather is attenuated gradually along its path until its depletion or until it leaves the enclosure. The locally absorbed fraction of the ray's energy contributes to the heat exchange rates of subvolumes along the ray's path. This method was also called "absorption suppression" by Walters and Buckius [6]. A large variety of problems of great complexity can be simulated with reasonable efficiency using either standard or energy partitioning methods in forward Monte Carlo simulations, when overall knowledge of the radiation field is desired.

The MCRT method has been applied to all aspects of radiative heat transfer [7,8]. In applications without a participating medium, ray tracing is relatively simple. However, in many high-temperature applications, such as combustion problems, participating media play a key role. A major difficulty is the evaluation of the optical thickness that a ray passes through, since the temperature and concentration fields tend to be highly inhomogeneous and turbulent. In traditional treatments the turbulence of temperature and concentrations is regarded as an uncoupled process from radiation, using mean temperature and concentrations to evaluate the radiative intensities and properties [9]. However, many experimental and numerical studies have demonstrated that radiative fluxes can be underestimated by a factor of up to 3, if mean temperature and concentration fields are employed [10,11]. Therefore, turbulence-radiation interactions have been considered in many recent combustion calculations. The treatment of turbulence-radiation interactions is not a trivial task because of the nonlinear coupling of temperature, species concentrations, and radiative intensities. Among various treatments of turbulence-radiation interactions, the joint-probability-density-function (joint-PDF) methods, such as the velocity-composition PDF [12] and the composition PDF [13] methods, are the most advanced and promising methods. In such methods, a particle Monte Carlo method [14] is frequently used to solve the transport equation of the joint PDF, in which the flow is represented by a sufficiently large number of discrete particles (point masses) evolving with time. In such flow fields, to apply the Monte Carlo method for radiation calculations, traditional contimuum ray-tracing models are no longer useful. No work appears to have been done to date to implement MCRT in media represented by discrete particle fields, which is the aim of the present paper.

While spectral variations of the absorption coefficient are an important aspect of radiation calculations, it is not the purpose of this paper to discuss spectral models. Therefore, the discussion will be limited to gray media, but the same analysis can readily be applied to nongray media.

2 Ray-Particle Interaction Models

To simulate the radiative transfer process by ray tracing in a discrete particle field, the interaction between infinitesimal point masses and infinitesimally thin photon rays needs to be modeled. This can be done by assigning effective volumes to the point masses, by assigning an influence volume to the ray's trajectory, or a combination of both. In this section, several particle models and ray models are developed first, followed by photon emission and absorption algorithms based on these models.

[1]To whom all correspondence should be addressed.

Contributed by the Heat Transfer Division of ASME for publication in the JOURNAL OF HEAT TRANSFER. Manuscript received October 3, 2005; final manuscript received March 21, 2006. Review conducted by Bakhtier Farouk.

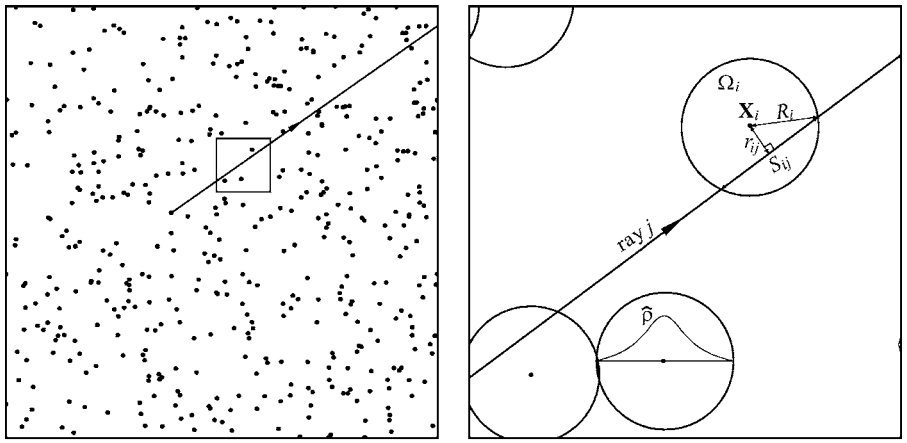

Fig. 1 (*a*) PPM representation of a 2D medium; (*b*) SPM representation of a sub-region in (*a*)

2.1 Particle and Photon Ray Models

2.1.1 Point Particle Model (PPM). In this model, particles are treated as point masses, i.e., they carry an amount of mass without a specific shape at a certain spatial location as shown in Fig. 1(*a*), which is a 2D particle field. The only geometric information known about the particles is their position vector. However, particles do have a nominal volume, which may be calculated from their thermophysical properties such as pressure and temperature. For example, if the ideal gas assumption is adopted, the nominal volume may be computed as

$$V_{o,i} = \frac{m_i R T_i}{p_i} \tag{1}$$

where m_i is the mass carried by particle i, T_i is its temperature, p_i is its total pressure, and R is the gas constant. To enforce consistency in the discrete particle representation of the medium, the overall nominal volume of all particles should be the same as the actual geometric expanse of the medium. As a consequence, one may regard the nominal volume of a particle as its real volume.

The point particle model only contains the particle information that the original discrete particle field contains. It does not employ any other assumption and, therefore, it will not induce any inconsistency. The disadvantage of this model is that it is difficult to determine the interaction of a photon ray with a volume without shape.

2.1.2 Spherical Particle Model. In this method, each point-mass m_i has a spherical influence region Ω_i, surrounding it as shown in Fig. 1(*b*). The mass is distributed to its influence region according to a density profile,

$$\hat{\rho}_i(\mathbf{x}) = \begin{cases} \rho_{o,i} W_{3D}\left(\dfrac{|\mathbf{x}-\mathbf{x}_i|}{R_i}\right), & |\mathbf{x}-\mathbf{x}_i| < R_i \\ 0, & |\mathbf{x}-\mathbf{x}_i| \geq R_i \end{cases} \tag{2}$$

where $\mathbf{x}_i$ is the spatial location vector of the point-mass i, R_i is its influence radius, $\rho_{o,i}$ is the nominal density calculated by

$$\rho_{o,i} = \frac{m_i}{V_{o,i}} = \frac{p_i}{R T_i} \tag{3}$$

and W_{3D} is a spherically symmetric weight function which decays from the center along radial directions and satisfies the condition

$$\int_{\Omega_i} W_{3D}\left(\frac{|\mathbf{x}-\mathbf{x}_i|}{R_i}\right) d\mathbf{x} = V_{o,i} \tag{4}$$

so that the total mass in the influence region is equal to the point mass. In this method, particles are assigned a spherical volume (influence region) with varying density, and overlapping other particles in the domain. This is called the *spherical particle method* (SPM).

One may adjust the size of influence region and the mass distribution of particles by employing different weight functions. Larger influence radii lead to more particle overlap and spatial gradients may be smoothed out. On the other hand, smaller influence radii result in smaller particle volumes, making it more difficult to interact with rays. The simplest possible weight function is

$$W_{3D}\left(\frac{|\mathbf{x}-\mathbf{x}_i|}{R_i}\right) = 1 \tag{5}$$

i.e., the density is constant in the influence region and its volume is the same as the nominal volume of the particle. The particles can then be regarded as constant density spheres with a radius determined by their nominal volumes,

$$R_i = \left(\frac{3 V_{o,i}}{4\pi}\right)^{1/3} \tag{6}$$

This model will be termed the *constant density sphere* (CDS) model. The overall density at an arbitrary position is the sum of density contributions from all nearby particles. Some locations may be influenced by more than one particle, while some other locations may not be in the influence region of any particle, i.e., there is a void in these places. Therefore, this model cannot recover a continuous density medium as shown in Fig. 1(*b*) and Fig. 2. Figure 1(*b*) is a small portion of the CDS representation of the 2D field given in Fig. 1(*a*) (if variable density were employed, the R_i would be larger, resulting in substantial overlap, even in this region of few particles). A location with lots of void space was chosen for simplicity in Fig. 1(*b*). In order to show particle locations in a plane, a 2D rather than 3D particle field is depicted. Figure 2 shows the density distribution on a cross-section of a 3D CDS representation of a homogeneous medium of unity density.

2.1.3 Line Ray Model. In this model, a ray is simply treated as a volume-less line and energy propagates one-dimensionally along the line. This is the standard model for ray tracing in continuous media. Since such rays are not designed to have a specific volume,

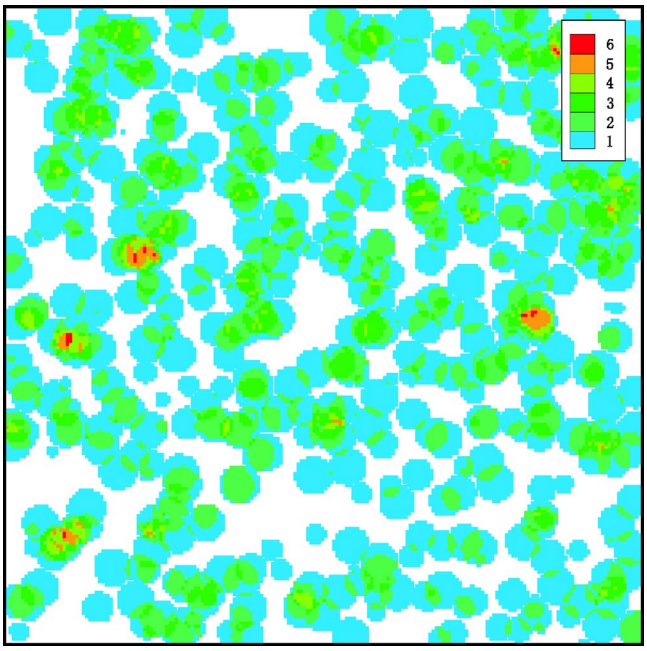

Fig. 2 Relative density distribution on a cross section of a 3D CDS representation for a homogeneous medium

they are not able to interact with point masses. Therefore, this model requires volumetric particle models for radiative transfer simulations.

2.1.4 Cone Ray Model. Physically, a photon bundle consists of many millions of individual photons, occupying a small solid angle. Thus, to model the volume of a ray, one may assign a small solid angle to the ray and treat it as a cone. Energy is assumed to propagate axisymmetrically along the cone, with its strength decaying in the radial direction normal to the cone axis, similar to the weight function assigned to particle density in Eq. (2), but in 2D. For a ray emitted at $\mathbf{x}_o$ into a direction given by a unit direction vector $\hat{\mathbf{s}}$, the intensity at location $\mathbf{x}$ in the ray can then be modeled as

$$I(s,r) = I_o(s) W_{2D}[r/R_c(s)] \tag{7}$$

where $s=(\mathbf{x}-\mathbf{x}_o)\cdot\hat{\mathbf{s}}$ is the distance from the emission location to a point on the ray axis, r is the distance from a point to the ray axis on a plane normal to the axis, $I_o(s)$ is the intensity at the ray center, and $R_c(s)$ is the local influence radius of the cross-section as depicted in Fig. 3. W_{2D} is a normalized two-dimensional center-symmetric profile which satisfies

$$\int_0^1 W_{2D}(r')2r'dr' = 1 \quad \text{and} \quad r' = r/R_c \tag{8}$$

Again, many weight functions are possible, ranging from $W_{2D}=1$ to Gaussian decay. A popular Gaussian-like weight function is provided here [15] as

$$W_{2D}(r') = \frac{60}{7}\begin{cases} \frac{1}{3} - 4r'^2 + 4r'^3, & 0 \le r' < \frac{1}{2} \\ \frac{4}{3}(1-r')^3, & \frac{1}{2} \le r' < 1 \\ 0, & r' \ge 1 \end{cases} \tag{9}$$

Physically, the distribution of energy emitted from a point is isotropic in all directions. Different rays from the same point may overlap if rays have a volume. The Gaussian decay of energy along the radial direction provides a smoother overlap than a uniform energy distribution across the cone cross section. Since in this model the ray has a specific volume, volume-less particles can be intercepted by the ray, and this model can work together with the point particle model.

2.2 Emission From a Particle. We now focus on the implementation of Monte Carlo methods for the simulation of radiative transfer in particle-based media, i.e., how photon bundles are emitted from the particle field, how they are traced, and how they interact with other particles.

A small gas volume emits energy uniformly into all directions. In Monte Carlo simulations, the total energy is divided into a number of photon bundles (rays), which are released into random directions. In a physical gas volume the emitted energy comes from every point in the volume. If the medium is represented by discrete particles, emission takes place inside these particles. Thus, depending on the optical thickness of the particle, and the point and direction of emission, some of the emitted energy may not escape from the particle due to self-absorption. If the particle is optically thin, the self-absorption of emission is negligible and the total emission from particle i is calculated from [1]

$$Q_{\text{emi},i} = 4\kappa_{\rho,i} m_i \sigma T_i^4 \tag{10}$$

where $\kappa_{\rho,i}$ is the density-based Planck-mean absorption coefficient at particle temperature T_i, σ is the Stefan-Boltzmann constant, and m_i is the mass. If self-absorption is considered and the particle is

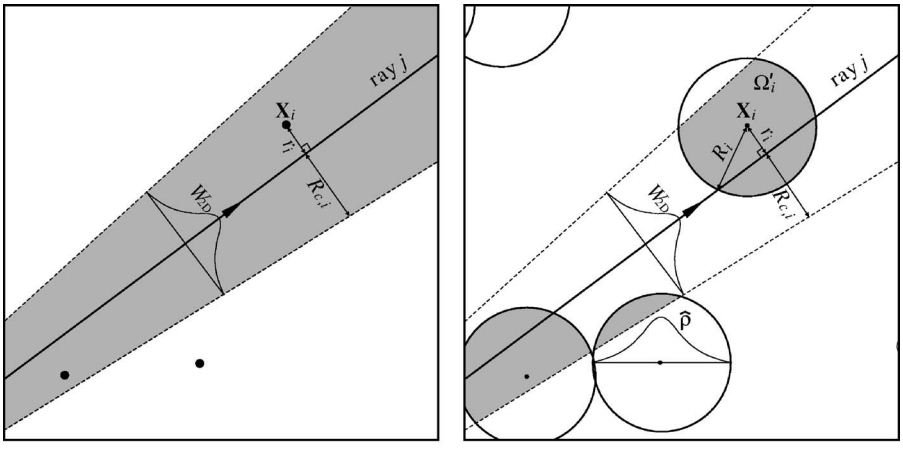

Fig. 3 (*a*) Cone-PPM scheme; (*b*) Cone-SPM scheme

assumed to be a constant density sphere, the total emission from a sphere is obtained from [1]

$$Q_{\text{emi},i} = 4\pi R_{o,i}^2 \sigma T_i^4 \left\{ 1 - \frac{1}{2\tau_{o,i}^2}[1 - (1 + 2\tau_{o,i})e^{-2\tau_{o,i}}] \right\} \quad (11)$$

where $R_{o,i} = (3V_{o,i}/4\pi)^{1/3}$ is the nominal spherical radius of particle i and $\tau_{o,i} = \rho_{o,i}\kappa_{\rho,i}R_{o,i}$ is the optical thickness of the spherical volume based on the nominal radius. In the point particle model, the shape of a particle is arbitrary, but Eq. (11) is still a good approximation of total emission from such a particle. If more than one ray is emitted from a particle, the sum of initial energy carried by all rays must be equal to the total emission calculated from Eq. (10) or Eq. (11), depending on whether self-absorption is neglected.

2.3 Absorption Models. The basic task of simulating the absorption of a photon bundle in a medium described by a point particle field is the evaluation of the optical thickness that a ray traverses along its path. This is achieved by modeling the interaction between the ray and the particles that it encounters. Based on different models employed for rays and particles, several schemes for absorption simulation may be obtained.

2.3.1 Line-SPM Scheme. In this scheme, the ray is treated as a line and the spherical particle model (SPM) is employed for the particles as shown in Fig. 1(*b*). The contribution of particle i to the optical thickness that ray j passes through is computed as

$$\Delta\tau_{ij} = \int_{S_{ij}} \hat{\rho}_i[\mathbf{x}(s)]\kappa_{\rho,i} ds \quad (12)$$

where s is the ray path coordinate as in Eq. (7), S_{ij} is the intersection of ray j and the influence region of particle i, $\kappa_{\rho,i}$ is the density-based absorption coefficient of particle i at its own temperature, and $\hat{\rho}_i$ is the local density of particle i as indicated in Fig. 1(*b*). If the constant density sphere (CDS) model is employed, the mass of the particle is distributed uniformly across its influence region and Eq. (12) can be simplified to

$$\Delta\tau_{ij} = 2\rho_{o,i}\kappa_{\rho,i}\sqrt{R_i^2 - r_{ij}^2} \quad (13)$$

where $\rho_{o,i}$ is the nominal density defined in Eq. (3), R_i is the influence radius, and r_{ij} is the distance from the center of particle i to ray j, as indicated in Fig. 1(*b*). Since Eq. (13) has a very simple form, its implementation can be very fast.

The total optical thickness that ray j passes through is simply the summation of the contributions from the individual particles it interacts with,

$$\tau_j = \sum_{i \in I_j} \Delta\tau_{ij} \quad (14)$$

where I_j denotes all the particles intersected by ray j.

2.3.2 Cone-PPM Scheme. If the ray is modeled as a cone, it is possible to let it interact with point particles. The energy change of a conical ray, when it traverses over a small distance ds in a continuous medium, is

$$dE(s) = -\int_0^{R_c} \kappa ds I(r) 2\pi r dr = -\bar{\kappa} ds \int_0^{R_c} I(r) 2\pi r dr = -E(s)\bar{\kappa} ds \quad (15)$$

where $E(s)$ is the plane-integrated energy over the cone cross-section at axial location s, κ is the local absorption coefficient, $\bar{\kappa}(s)$ is the plane-averaged absorption coefficient, and $R_c(s)$ is the local radius of the cross-section. From Eqs. (15), (7), and (8), the plane-averaged absorption coefficient can be derived as

$$\bar{\kappa} = \frac{\int_0^{R_c} \kappa I r dr}{\int_0^{R_c} I r dr} = \frac{\int_0^1 \kappa I r' dr'}{\int_0^1 I r' dr'} = \frac{\int_0^1 \kappa W_{2D} 2r' dr'}{\int_0^1 W_{2D} 2r' dr'} = \int_0^1 \kappa W_{2D} 2r' dr' \quad (16)$$

Therefore, the total optical thickness that the ray passes through along its path S is

$$\tau = -\ln\frac{E(s)}{E(0)} = -\int_S \frac{dE}{E} = \int_S \bar{\kappa} ds = \int_S \int_0^1 \kappa W_{2D} 2r' dr' ds$$
$$= \int_S \int_0^{R_c} \frac{\kappa W_{2D}}{\pi R_c^2} 2\pi r dr ds = \int_V \frac{\kappa W_{2D}}{\pi R_c^2} dV \quad (17)$$

where V is the volume that the ray covers in its path.

In discrete particle fields as shown in Fig. 3(*a*) the absorption coefficient is represented by a set of delta functions,

$$\kappa = \sum_i \kappa_i V_i \delta(\mathbf{x} - \mathbf{x}_i) \quad (18)$$

Integration over V yields

$$\tau = \sum_{i \in I} \frac{\kappa_i W_i V_i}{\pi R_{c,i}^2} = \sum_{i \in I} \frac{\kappa_{\rho,i} W_i m_i}{\pi R_{c,i}^2} \quad (19)$$

where I denotes all the particles enclosed by the cone. For point particles, the particle weight is a point weight in the energy distribution, i.e.,

$$W_i = W_{2D}(r_i/R_{c,i}) = W_{2D}(r_i') \quad (20)$$

where r_i' is the distance from particle i to the cone axis, normalized by the local cone radius $R_{c,i}$.

2.3.3 Cone-SPM Scheme. In the most advanced scheme, the ray is treated as a cone, and the particle is given a specific shape and a density distribution may exist across its volume, as shown in Fig. 3(*b*). In this case, the weight function and absorption coefficient cannot be separated from the volume integral in the optical thickness evaluation. The total optical thickness passed through by a ray is obtained as

$$\tau = \sum_{i \in I} \kappa_{\rho,i} \int_{\Omega_i'} \frac{\hat{\rho}_i W_{2D}[r/R_c(s)]}{\pi R_c^2(s)} d\mathbf{x} \quad (21)$$

where Ω_i' is the intersection of the particle influence region and the ray, r is the distance from a location in Ω_i' to the cone axis and $R_c(s)$ is the local cone radius at this location. Since the solid angle of the ray is small, $R_c(s)$ can be regarded as constant in a single particle, i.e., the small cone segment interacting with a particle can be treated as a small cylinder. Then the local radius $R_c(s) \equiv R_{c,i}$ can be separated from the integral,

$$\tau \simeq \sum_{i \in I} \frac{\kappa_{\rho,i}}{\pi R_{c,i}^2} \int_{\Omega_i'} \hat{\rho}_i(\mathbf{x}) W_{2D}(r/R_{c,i}) d\mathbf{x} \quad (22)$$

For constant-density spherical particles this reduces to

$$\tau = \sum_{i \in I} \frac{\kappa_i}{\pi R_{c,i}^2} \int_{\Omega_i'} W_{2D}(r/R_{c,i}) d\mathbf{x}$$
$$= \sum_{i \in I} \frac{\kappa_i}{\pi R_{c,i}^2} \int_{r_{\min}}^{r_{\max}} W_{2D}(r/R_{c,i}) A_i(r) dr$$
$$= \sum_{i \in I} \frac{\kappa_i R_{c,i}}{\pi} \int_{r_{\min}'}^{r_{\max}'} W_{2D}(r') A_i'(r') dr' \quad (23)$$

where $r'=r/R_{c,i}$ is the normalized distance from a point in Ω_i' to the cylinder (cone) axis, $r'_{\min}$ is the normalized closest distance and $r'_{\max}$ is the farthest. All points of the same distance r' are part of a cylindrical shell $A_i(r')$ around the cone axis, and its normalized form can be evaluated as

$$A_i'(r') = \frac{A_i(r')}{R_{c,i}^2} = \begin{cases} 4r'^{3/2} r_i'^{1/2} \alpha^{1/2} E(1/\alpha), & r' \le R_i' - r_i' \\ 8r'^{3/2} r_i'^{1/2} [2E(\alpha) - \beta K(\alpha)], & r' > R_i' - r_i' \end{cases} \tag{24}$$

where $r_i'=r_i/R_{c,i}$ is the normalized distance from the particle center to the cylinder axis, $R_i'=R_i/R_{c,i}$ is the normalized radius of particle i, K and E are complete elliptic integrals of the first and second kind [16], and

$$\alpha = [R_i'^2 - (r' - r_i')^2]/4r'r_i'$$

$$\beta = [(r' + r_i')^2 - R_i'^2]/2r'r_i' \tag{25}$$

If we define

$$f_i = \frac{1}{\pi} \int_{r'_{\min}}^{r'_{\max}} W_{2D}(r') A_i'(r') dr' \tag{26}$$

Eq. (23) can be rewritten as

$$\tau = \sum_{i \in I} \kappa_i R_{c,i} f_i \tag{27}$$

Rather than making costly evaluations during the simulation, Eq. (26) can easily be tabulated as a function of the two dimensionless parameters r_i' and R_i'.

3 Sample Calculations

In order to evaluate and compare the performance of the different schemes for Monte Carlo ray tracing in media represented by statistical particles, one-dimensional radiative heat transfer problems in a nonscattering gray gaseous medium are studied. Two media will be considered: a 1D gas slab bounded by two infinitely large, parallel, cold, black walls and a gas sphere surrounded by a cold black wall. The thickness of the slab is fixed at $L=10$ cm and the radius of the sphere is $R=5$ cm. The temperature and density (or absorption coefficient) may vary across the slab thickness or along the sphere radial direction. The resulting radiative heat flux at the boundary ($x=0$, L for slab; $r=R$ for sphere) can be evaluated exactly through numerical integration [1].

In the slab problem, the 1D medium is simulated by repeating a gas cube, each with equal side lengths of 10 cm in the two infinite dimensions. A single gas cube is then taken as the computational domain in the Monte Carlo simulation. In the sphere problem, the computational domain is the gas sphere itself. The continuous gas medium in both problems is represented by a number of discrete gas particles randomly placed inside the computational domain. The mass of particles can be equally sized or have a distribution function. For computational efficiency, a mesh of cubic cells is laid on top of the computational domain because the ray-tracing algorithm on smaller cubic cells is simpler and more efficient. The same cubic-cell mesh is used for the sphere problem as well, by first identifying a $D \times D \times D$ cube enclosing the sphere, then dividing the cube into cubic cells, where $D=2R$ is the diameter of the sphere. In the slab problem each of the cells contains a number of gas particles, while in the sphere problem some cells at the corners of the mesh may contain no particles, because they may be outside the spherical computational domain. If the point particle model (PPM) is employed, it can be assumed that each particle is completely enclosed by a single cell, since the shape of particles is not specified. However, if the spherical particle model (SPM) is employed, the cells contain not only the particles with their center in it, but also parts of particles from neighboring cells.

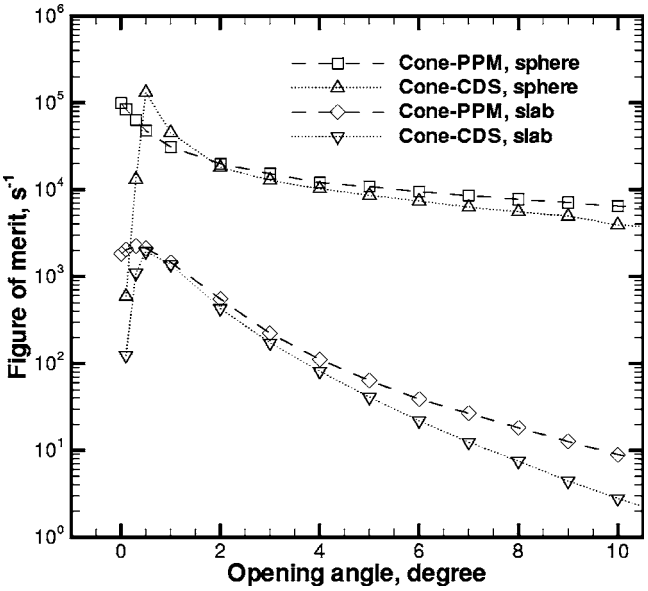

Fig. 4 Figure of merit (FoM) of cone ray models at different cone opening angles; 50×10,000 equally sized particles; 1 ray/particle; homogeneous medium

Thus, a scheme must be developed to avoid having the ray interact with a single particle more than once, since a single particle may belong to multiple cells.

When the cone ray model is adopted for ray tracing, the opening angle (the angle between the cone axis and its lateral surface) needs to be chosen. Larger opening angles result in more particles caught by the ray, requiring more CPU time per ray. At the same time, larger opening angles reduce the statistical scatter (i.e., reduce the number of required photon bundles for a given desired standard deviation), while also smoothing gradients that may exist in the solution. In turbulent flow fields large opening angles, therefore, may smooth out the turbulence. The "figure of merit" (FoM) of a Monte Carlo simulation is defined as [17]

$$\text{FoM} = \frac{1}{\epsilon^2 t}, \quad \epsilon = \left(\frac{1}{S} \sum_{s=1}^{S} (q_s/q^o - 1)^2 \right)^{1/2} \tag{28}$$

where ϵ is the root-mean-square (rms) relative error of the simulation and t is the simulation time. In the current work, the error of 50 simulations is adopted for ϵ ($S=50$); q_s is the simulation result of radiative flux at the boundary and q^0 is the exact solution found in Chapter 9 of Ref. [1]. A good Monte Carlo simulation should have a high FoM score. Figure 4 shows FoM scores for different opening angles. The gas slab or sphere was represented by 10,000 randomly distributed, equally sized particles, each of which emits all its energy into a single random direction. Temperature and absorption coefficient are uniform and, thus, the smoothing effect of larger cone angles is not an issue. The mesh in use contains $5 \times 5 \times 5 = 125$ cubic cells. As seen from Fig. 4, for this one-dimensional problem 1 deg is the optimal opening angle, which can achieve high accuracy as well as high CPU efficiency. Although smaller opening angles required less computational time, their errors were larger, because they could not interact with enough particles. Similar results were also obtained for other temperature and absorption coefficient profiles. Therefore, for all the following simulations in this paper, an opening angle of 1 deg is chosen, whenever the cone ray model is employed.

Another factor that can affect the simulation speed is the number of particles per cell. When a ray is traced, the cells that it travels through are identified first. Then all particles in those cells are checked for interaction with the ray. For a finer mesh, the number of particles per cell is smaller and, thus, a smaller number

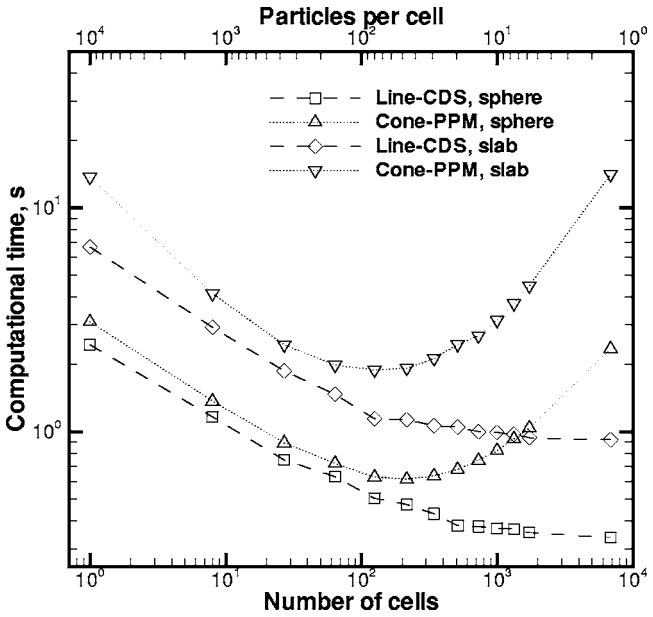

Fig. 5 Computational time at different particle number densities; 50×10,000 equally sized particles; 1 ray/particle; homogeneous medium

of particles are checked during ray tracing. However, more cells must be searched. Thus, finer meshes tend to reduce the time spent on checking particles for their interaction with a ray, but increase the overhead related to cell searching and recording. Therefore, an optimal value of the number of particles per cell may exist. Figure 5 shows the computational time for different cell sizes, keeping the total number of particles in the domain constant. Results for the cone-CDS scheme are not shown to retain readability, and are essentially the same as those for the cone-PPM scheme, since both schemes share the same algorithm except for the particle weight, which has only a very small impact on computational time. From Fig. 5 it is seen that no optimal cell size exists for the line-CDS scheme; the computational time decreases consistently with decrease of cell size. Therefore, the optimum value for the number of particles per cell is 1 particle/cell, which has been verified for up to 100,000 particles in the domain. For cone schemes, however, an optimal value was found to be around 50 particles/cell in both the slab and the sphere problems. In the line scheme rays are one-dimensional lines. The number of cells that a ray intersects is proportional to the number of cells in one dimension, i.e., the cubic root of the number of cells in the 3D computational domain. Doubling the number of cells in each dimension, the number of cells to be searched is doubled, but the number of particles to be checked for interaction becomes only one-eighth of the original number. In cone schemes, on the other hand, rays are assigned a volume. The number of cells that a ray intersects increases rapidly with increase of the number of cells. If the cell size is too small, the speed-up gained by checking fewer particles cannot compete with the overhead related to cell searching and recording and, thus, an optimal cell size exists for cone schemes.

Several combinations of temperature profiles and absorption coefficient profiles have been tested as listed in Table 1, with different cases numbered in Table 2. In those profile equations x and L denote the x position and the slab thickness in the slab problem, and the r variable and the sphere radius in the sphere problem. The three absorption schemes have been implemented and compared with exact solutions of boundary fluxes for all nine cases. Table 3 shows the corresponding root-mean-square (rms) relative error of 50 simulations in each case, in which the gas cube or sphere is represented by 10,000 equally sized random particles, each of which emits all its energy in a single ray into a random

Table 1 Temperature and absorption coefficient profiles

	Temperature profiles, K
const	$T(x)=T_o$
linear	$T(x)=T_o+(x/L)(T_L-T_o), \quad T_L/T_o=2$
sine	$T(x)=T_o+T_A\sin(2\pi x/L), \quad T_L/T_o=0.5$
	Absorption coefficient profiles, cm^{-1}
const	$\kappa(x)=0.1$
linear	$\kappa(x)=0.01+0.99(x/L)$
sine	$\kappa(x)=0.55+0.45\sin(2\pi x/L)$

direction. Since the slab has two boundaries, the result shown here is the averaged error of both boundaries. As shown in Table 3, the three absorption schemes have the same level of accuracy, especially in the slab problem. In the sphere problem the cone-PPM scheme achieves much better accuracy than the line-CDS scheme, but this improvement of accuracy comes at a cost of increased CPU time. As expected, the cone-CDS scheme has slightly better accuracy than the cone-PPM scheme, however, this also comes at a cost in slightly increased CPU time. Therefore, the three absorption schemes are essentially equivalent.

It is worth noting that the discrete particle representation of a continuous medium inevitably introduces a bias on radiation calculations when the density field cannot be recovered exactly. In the current sample problems the random distribution of particles inevitably generates fluctuations on the original homogeneous density fields, as shown in Fig. 2. Table 4 shows relative errors and standard deviations of all nine cases for the sphere problem. The negative sign attached to all errors indicates that the particle representation tends to underpredict the boundary flux. If the magnitude of the error is larger than or comparable with the standard deviation, the bias introduced by the particle representation is the major source of error. The bias is not so prominent in the slab problem as in the sphere problem, which can be seen from Fig. 6, which shows the variation of rms error with respect to the number of rays each particle emits. The particles are all of the same size and only the result of Case (1) is provided for clarity. The relation follows the inverse-square-root law in the slab problem, indicating that standard deviation is the major source of rms error. In contrast, the relation does not follow the inverse-square-root law in the sphere problem, indicating that bias is an important contributor to the error. Similarly, Fig. 7 shows the relation between the rms error and the number of particles, with which the medium in

Table 2 Case numbering

Case	(1)	(2)	(3)	(4)	(5)	(6)	(7)	(8)	(9)
T	const	const	const	linear	linear	linear	sine	sine	sine
κ	const	linear	sine	const	linear	sine	const	linear	sine

Table 3 Percentage rms errors of radiative fluxes at boundaries; 50×10,000 particles; 1 ray/particle; 125 cells; uniform particle mass

	Line-CDS		Cone-PPM		Cone-CDS	
Case No.	Slab	Sphere	Slab	Shpere	Slab	Sphere
(1)	1.621	1.148	1.509	0.702	1.516	0.564
(2)	1.574	1.044	1.542	0.783	1.498	0.574
(3)	1.821	0.730	1.729	0.664	1.733	0.536
(4)	1.975	1.258	1.974	0.899	1.880	0.741
(5)	2.027	1.191	1.986	0.969	1.935	0.758
(6)	1.784	0.807	1.837	0.778	1.782	0.680
(7)	2.098	1.115	2.000	0.852	2.007	0.771
(8)	1.798	1.006	1.798	0.838	1.787	0.702
(9)	2.341	1.352	2.180	1.346	2.191	1.273

Table 4 Percentage errors and standard deviations of radiative fluxes at the boundary in the sphere problem; 50×10,000 particles; 1 ray/particle; 125 cells; uniform particle mass

	Line-CDS		Cone-PPM		Cone-CDS	
Case No.	Error	STD	Error	STD	Error	STD
(1)	−1.113	0.288	−0.637	0.298	−0.487	0.288
(2)	−1.003	0.293	−0.722	0.305	−0.495	0.295
(3)	−0.564	0.468	−0.454	0.490	−0.262	0.473
(4)	−1.149	0.517	−0.730	0.530	−0.533	0.520
(5)	−1.066	0.537	−0.799	0.553	−0.536	0.542
(6)	−0.516	0.627	−0.461	0.633	−0.273	0.629
(7)	−0.841	0.739	−0.329	0.794	−0.223	0.746
(8)	−0.800	0.617	−0.548	0.640	−0.341	0.620
(9)	−0.495	1.271	−0.302	1.325	−0.048	1.286

the gas cube is represented. Again, it is observed that the relation follows the inverse-square-root law for the slab problem but not for the sphere problem. The bias is caused by the representation of a homogeneous or gradually varying density field by a fluctuating density field. In turbulent flow simulations the inhomogeneous particle field is assumed to provide a snapshot of a turbulent medium, and no bias exists.

The effect of varying particle size was also investigated. In the slab problem a linear distribution of particle mass along the x direction is considered, i.e.,

$$m(x) = m_o + (m_L - m_o)(x/L) \tag{29}$$

where m_o and m_L are the values of particle mass at the two boundaries $x=0$ and $x=L$. Because the probability distribution $P(x)$ associated with particle mass distribution $m(x)$ is inversely proportional to $m(x)$, the following random number relation holds for the x coordinate of random particle positions

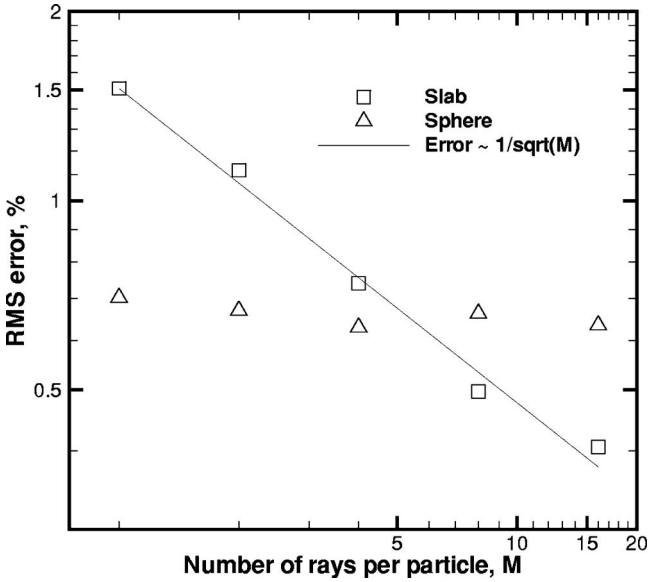

Fig. 6 Averaged boundary flux error versus number of rays per particle; cone-PPM scheme; 50×10,000 particles; uniform particle mass; Case (1)

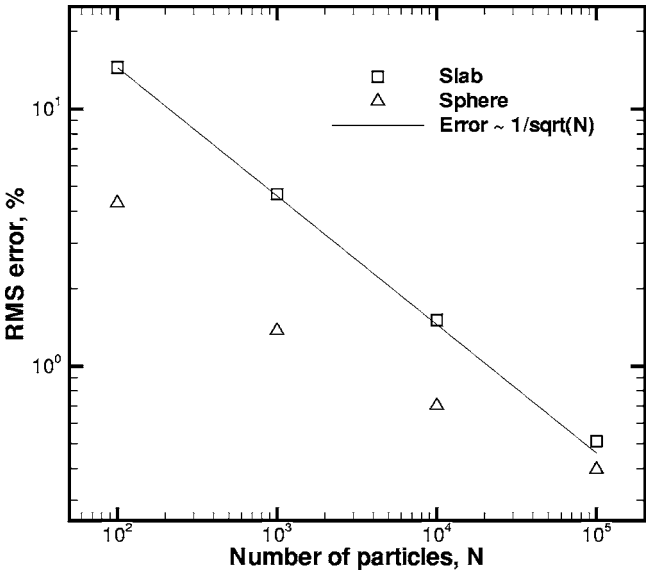

Fig. 7 Averaged boundary flux error versus number of particles in computation domain; cone-PPM scheme with one ray per particle; 50×*N* particles; uniform particle mass; Case (1)

$$\eta_x = \frac{\int_0^x P(x)dx}{\int_0^L P(x)dx} = \frac{\int_0^x 1/m(x)dx}{\int_0^L 1/m(x)dx} = \frac{\int_0^x [m_o + (m_L - m_o)(x/L)]^{-1}dx}{\int_0^L [m_o + (m_L - m_o)(x/L)]^{-1}dx} \tag{30}$$

where η_x is a random number uniformly distributed in $[0,1)$. After carrying out the integrations and rearranging, one obtains

$$x = \frac{(m_L/m_o)^{\eta_x} - 1}{(m_L/m_o) - 1} L \tag{31}$$

where (m_L/m_o) is the mass ratio of particles at $x=L$ to that at $x=0$. Since there is no variation in the y and z directions, the y and z coordinates of particle positions can be readily generated as

$$y = \eta_y L, \quad z = \eta_z L \tag{32}$$

where η_y and η_z are two additional independent random numbers uniformly distributed in $[0,1)$. Figure 8 shows a 2D CDS representation with a linear particle mass distribution for a homogeneous medium.

Table 5 gives the results for the linear particle mass distribution. For all nine cases, the random number sequence used in the generation of particle position and emission direction is the same as in the uniform mass cases. Again, the three absorption schemes all achieve the same level of accuracy. Comparing Table 5 to 3, it is observed that the difference caused by varying the particle masses is fairly small considering that particle mass across the domain varies by a factor of 1000. It is also noticed that the error at $x=L$ is larger than at $x=0$. This is because particles are larger near that boundary, but still emit only one ray per particle as do the smaller particles near the boundary at $x=0$. It also explains why errors for the linear temperature profile are higher than for other profiles. In that scenario larger particles are at higher temperatures and the importance of emission from larger particles is even more crucial to the simulation result.

4 Summary

For radiative heat transfer simulations using Monte Carlo ray tracing in media represented by discrete particle fields it is important to find ways to model the interaction between point masses

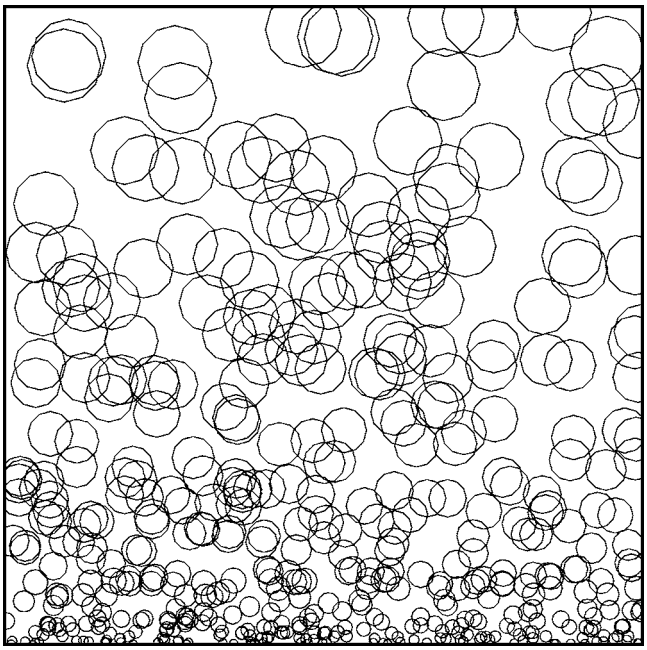

Fig. 8 2D CDS representation with linear mass distribution for a homogeneous medium

and photon rays. In the point particle model (PPM) the shape of particles is not presumed in order to avoid any inconsistency with the underlying particle field. As a result, this method is limited to applications, in which the ray has a shape and volume. In the spherical particle model (SPM) particles are assumed to be spheres. As a special case, in the constant density sphere (CDS) model the density is assumed to be constant across the entire particle volume. Although it is easy to interact spheres with a ray, this model introduces some inconsistencies. For example, it cannot recover continuous medium properties due to the existence of particle overlap and voids.

In the line ray model for photon bundles, rays are simply treated as volume-less lines and energy propagates one-dimensionally along those lines. In the cone ray model each ray is assigned a small solid angle, and is thus treated as a cone; energy propagates two-dimensionally. The strength of the ray may vary across the cross-section of the cone through a given weight function. Since the ray has a volume, it is possible to have the ray interact with volume-less particles directly. Thus, three schemes for the interaction between ray and particles, i.e., line-CDS, cone-PPM and cone-CDS schemes, have been proposed and examined in two one-dimensional radiative heat transfer problems with various temperature and absorption coefficient profiles. It was shown that all three schemes achieved comparable levels of accuracy. For the cone approaches, an optimal opening angle was found, and a most efficient number of particles per cell exists. For the line approach, computational speed increases consistently with decrease of the number of particles per cell.

Table 5 Percentage rms errors of radiative fluxes at slab boundaries; 50×10,000 particles; 1 ray/particle; volume ratio: $m_L/m_o=1000$

	Line-CDS		Cone-PPM		Cone-CDS	
Case No.	$x=0$	$x=L$	$x=0$	$x=L$	$x=0$	$x=L$
(1)	1.896	3.378	1.958	3.173	1.956	3.123
(2)	2.795	3.671	2.864	3.675	2.862	3.685
(3)	1.863	2.234	1.985	2.162	1.939	2.146
(4)	4.050	4.332	3.956	4.493	3.656	4.513
(5)	4.584	4.740	4.623	4.947	4.581	4.910
(6)	3.748	3.990	3.727	4.025	3.596	4.009
(7)	2.174	4.412	2.225	3.593	2.208	2.819
(8)	2.398	3.647	2.522	3.016	2.481	2.905
(9)	2.377	2.487	2.443	2.471	2.396	2.417

Acknowledgment

This research has been sponsored by National Science Foundation under Grant No. CTS-0121573.

Nomenclature

A = cylindrical shell
I = emission intensity; particles enclosed by ray
L = thickness of gas slab; side length of computational domain
Q_{emi} = total energy emitted from a particle
R = particle influence radius; gas constant
R_c = local radius of cone
S = ray path; number of simulations
T = temperature
V_o = nominal volume of particle
W = weight function
m = particle mass
p = total pressure
q = heat flux
q^o = exact solution of heat flux
r = distance to axis of conical ray
r' = normalized distance to ray axis, r/R_c
s = axial distance from emission point
$\mathbf{x}$ = location vector
Ω = particle influence region
Ω' = particle influence region intercepted by ray
κ = linear absorption coefficient
κ_ρ = density-based absorption coefficient
η = random number
ρ_o = nominal density of particle
$\hat{\rho}$ = density profile in particle influence region
τ = optical thickness

Superscripts

$'$ = quantity normalized by local cone radius R_c

Subscripts

i = particle
j = ray
s = simulation
2D,3D = dimension of weight function

References

[1] Modest, M. F., 2003, *Radiative Heat Transfer*, 2nd ed., Academic, New York.
[2] Heinisch, R. P., Sparrow, E. M., and Shamsundar, N., 1973, "Radiant Emission From Baffled Conical Cavities," J. Opt. Soc. Am., **63**(2), pp. 152–158.
[3] Shamsundar, N., Sparrow, E. M., and Heinisch, R. P., 1973, "Monte Carlo Solutions—Effect of Energy Partitioning and Number of Rays," Int. J. Heat Mass Transfer, **16**, pp. 690–694.
[4] Modest, M. F., and Poon, S. C., 1977, "Determination of Three-Dimensional Radiative Exchange Factors for the Space Shuttle by Monte Carlo," ASME paper No. 77-HT-49.
[5] Modest, M. F., 1978, "Determination of Radiative Exchange Factors for Three Dimensional Geometries With Nonideal Surface Properties," Numer. Heat Transfer, **1**, pp. 403–416.
[6] Walters, D. V., and Buckius, R. O., 1992, "*Monte Carlo Methods for Radiative Heat Transfer in Scattering Media*," in Annual Review of Heat Transfer, Vol. 5, Hemisphere, New York, pp. 131–176.
[7] Howell, J. R., 1998, "The Monte Carlo Method in Radiative Heat Transfer," ASME J. Heat Transfer, **120**(3), pp. 547–560.
[8] Farmer, J. T., and Howell, J. R., 1998, "*Monte Carlo Strategies for Radiative Transfer in Participating Media*," In Advances in Heat Transfer, 34, J. P. Hartnett, and T. F. Irvine, eds., Academic, New York.
[9] Viskanta, R., and Mengüç, M. P., 1987, "Radiation Heat Transfer in Combustion Systems," Prog. Energy Combust. Sci., **13**, pp. 97–160.
[10] Faeth, G. M., Gore, J. P., Chuech, S. G., and Jeng, S. M., 1989, "*Radiation From Turbulent Diffusion Flames*," In Annual Review of Numerical Fluid Mechanics and Heat Transfer, 2, Hemisphere, Washington, D.C., pp. 1–38.

[11] Kounalakis, M. E., Gore, J. P., and Faeth, G. M., 1988, "*Turbulence/Radiation Interactions in Nonpremixed Hydogen/Air Flames*," In Twenty-Second Symposium (International) on Combustion, The Combustion Institute, pp. 1281–1290.
[12] Mazumder, S., and Modest, M. F., 1999, "Turbulence–Radiation Interactions in Nonreactive Flow of Combustion Gases," Int. J. Heat Mass Transfer, **121**, pp. 726–729.
[13] Li, G., and Modest, M. F., 2002, "Application of Composition PDF Methods in the Investigation of Turbulence–Radiation Interactions," J. Quant. Spectrosc. Radiat. Transf., **73**(2–5), pp. 461–472.
[14] Pope, S. B., 1985, "PDF Methods for Turbulent Reactive Flows," Prog. Energy Combust. Sci., **11**, pp. 119–192.
[15] Liu, G. R., and Liu, M. B., 2003, *Smoothed Particle Hydrodynamics—A Meshfree Particle Method*, World Scientific, Singapore.
[16] Abramowitz, M., and Stegeun, I. A., eds., 1965, *Handbook of Mathematical Functions*, Dover, New York.
[17] Lewis, E. E., and Miller, W. F., Jr., 1984, *Computational Methods of Neutron Transport*, Wiley, New York.